



ORIGINAL RESEARCH ARTICLE

Effect of Tool Travel Rate on Microstructure Evolution and Mechanical Properties of Dissimilar Friction Stir Welded Joints of AA7075 and AA6061 Aluminium Alloys

Rajeev Rana, Anish Karmakar, and D.B. Karunakar

Submitted: 8 January 2023 / Revised: 21 June 2023 / Accepted: 8 September 2023

The current research aims to investigate how processing parameters influence the mechanical properties and microstructure development of dissimilar AA7075/AA6061. These alloys were friction stir welded (FSWed) at varied traverse rates (ranging from 20 to 60 mm/min) while maintaining a constant rotation rate of 708 rpm. Several characterization techniques, such as electron microscopy and optical microscopy, were utilized to quantify the microstructure evolution of these dissimilar FSWed joints. A universal testing machine and a Vickers microhardness tester were used to evaluate the mechanical characteristics. The field emission-scanning electron microscope was used to examine the fracture surfaces of the fractured tensile specimens. The experiment revealed that the grain size within the nugget zone decreased as the tool traverse rate increased from 20 to 60 mm/min. Specifically, the grain size in the nugget zone measured $5.82 \mu\text{m}$ at a speed of 20 mm/min, whereas it reduced to $3.64 \mu\text{m}$ at 60 mm/min. Furthermore, the FSWed sample processed at 60 mm/min demonstrated a superior ultimate tensile strength of 251 MPa. The hardness values exhibited a similar increasing trend as the traverse speed increased. The heat-affected zone of the AA6061 side achieved the lowest hardness at a traverse rate of 20 mm/min. A ductile fracture mode predominated for most of the dissimilar joint fracture surfaces investigated.

Keywords dissimilar Al alloys, fractography, friction stir welding, mechanical properties, microstructure, onion ring

1. Introduction

Traditionally, the automotive sectors were the most prominent applications for aluminium (Al) alloys (Ref 1-3). However, Al alloy applications have spread into aviation and the military areas (Ref 4, 5) owing to their advantageous qualities such as lightweight, strength-to-weight ratio, low density, toughness and excellent corrosion resistance. (Ref 6, 7). A lot of studies have been performed to investigate 7xxx and 6xxx series Al alloys (Ref 8-10) for various applications because of their eutectic structure at elevated temperatures (Ref 11, 12). AA7075 alloy possesses superior mechanical performance, corrosion resistance, and low density. It is often used to fabricate upper wing structural components, the tail of an airplane, fins and aviation control surfaces (Ref 13-15).

On the other hand, AA6061 has outstanding welding performances and characteristics. It is commonly used for traditional structural parts, machinery, marine and process

equipment applications (Ref 16). A combination of both series of aluminium alloys could improve structural components' performance in the aircraft and automotive sectors (Ref 17, 18). However, joining dissimilar Al alloys is challenging owing to changes in chemical, mechanical, and physical properties which may result in intermetallic phase formation in the fusion zone (Ref 19, 20). Traditional welding techniques such as tungsten inert gas (TIG) and metal inert gas (MIG) welding have been frequently used for lightweight materials. However, they produce typical dendritic microstructure, solid-state porosity and cracks in the welded region, which diminishes the mechanical characteristics (Ref 21). Among all the welding techniques that have been used for joining light materials, Friction stir welding (FSW) has garnered more attention due to its ability to create sound welded joints when employing optimized process parameters (Ref 22). FSW is a solid-state welding method invented and patented by Thomas at The Welding Institute (TWI) (Ref 23). This process employs a non-consumable rotating tool that plunges into the material's attribute surface to be welded (Ref 24). During the FSW process, different zones are formed. These are the base metal (BM), stir zone/nugget zone (SZ/NZ), heat-affected zone (HAZ), and thermo-mechanically affected zone (TMAZ).

Numerous studies have previously studied the Friction Stir Welded (FSWed) joints of dissimilar Al alloys (Ref 25-30). Giraud et al. (Ref 31) investigated the intermixing behavior of Al alloy in NZ of dissimilar FSWed joints of AA7020 and AA6060. They examined that increasing traverse speed enhanced the grain refinement in the nugget at the AA6060 side. Srinivasan et al. (Ref 32) reported recrystallized and magnificent equiaxed grain structure in the NZ of FSWed joint of dissimilar AA6061/AA7075 Al alloys. Even after grain

Rajeev Rana and **D.B. Karunakar**, Department of Mechanical and Industrial Engineering, Indian Institute of Technology Roorkee, Roorkee, Uttarakhand 247667, India; and **Anish Karmakar**, Department of Metallurgical and Materials Engineering, Indian Institute of Technology Roorkee, Roorkee, Uttarakhand 247667, India. Contact e-mail: benny.karunakar@me.iitr.ac.in.

refinement, some variation was found throughout the NZ, which may correlate with the respective BM's original grain sizes. Ilangoan et al. (Ref 33) investigated the microstructural characteristics of dissimilar FSWed joints of AA5086/AA6061 Al alloys. They correlated the tensile properties with microstructural features and microhardness. They observed that the brittle intermetallic phases and higher grain boundary fraction near the weld enhance the hardness. The transition of strengthening phases in precipitation-hardening alloys should be a concern. Olea (Ref 34) and Sato (Ref 35) reported that 6XXX alloy wholly dissolved in the NZ during the FSW process to form supersaturated solid solutions. Niu et al. (Ref 36) found a highly inhomogeneous microstructure developed throughout the FSWed joint of dissimilar AA5083 and AA2024

Al alloys. They performed a comprehensive electron backscattered diffraction (EBSD) analysis throughout the surface of the FSWed joint. They reported that refined grains were observed in the nugget region and tilted elongated grains in the TMAZ region. However, Cabibo (Ref 37) reported a coarse equilibrium β phase in NZ during the FSW of AA6056. Reynold (Ref 38) found that the precipitates dissolved partially or wholly in the NZ of the FSWed joint of AA7050.

Until now, a limited amount of study has been conducted on dissimilar heat-treatable aluminum alloy FSWed joints. Moreover, little literature is available on the detailed microstructure behavior and mechanical characteristics of the dissimilar FSWed joints of AA6061/AA7075. Therefore, in this study, the microstructure characteristics of the welded joints of

Table 1 Chemical compositions of AA6061 and AA7075 aluminium alloys

Al alloys	Chemical composition (wt.%)								
	Si	Mn	Cu	Fe	Mg	Zn	Cr	Ti	Al
AA6061	0.68	0.07	0.32	0.68	0.98	0.21	0.18	0.09	Balance
AA7075	0.035	0.58	1.65	0.17	2.43	5.67	0.16	0.048	Balance

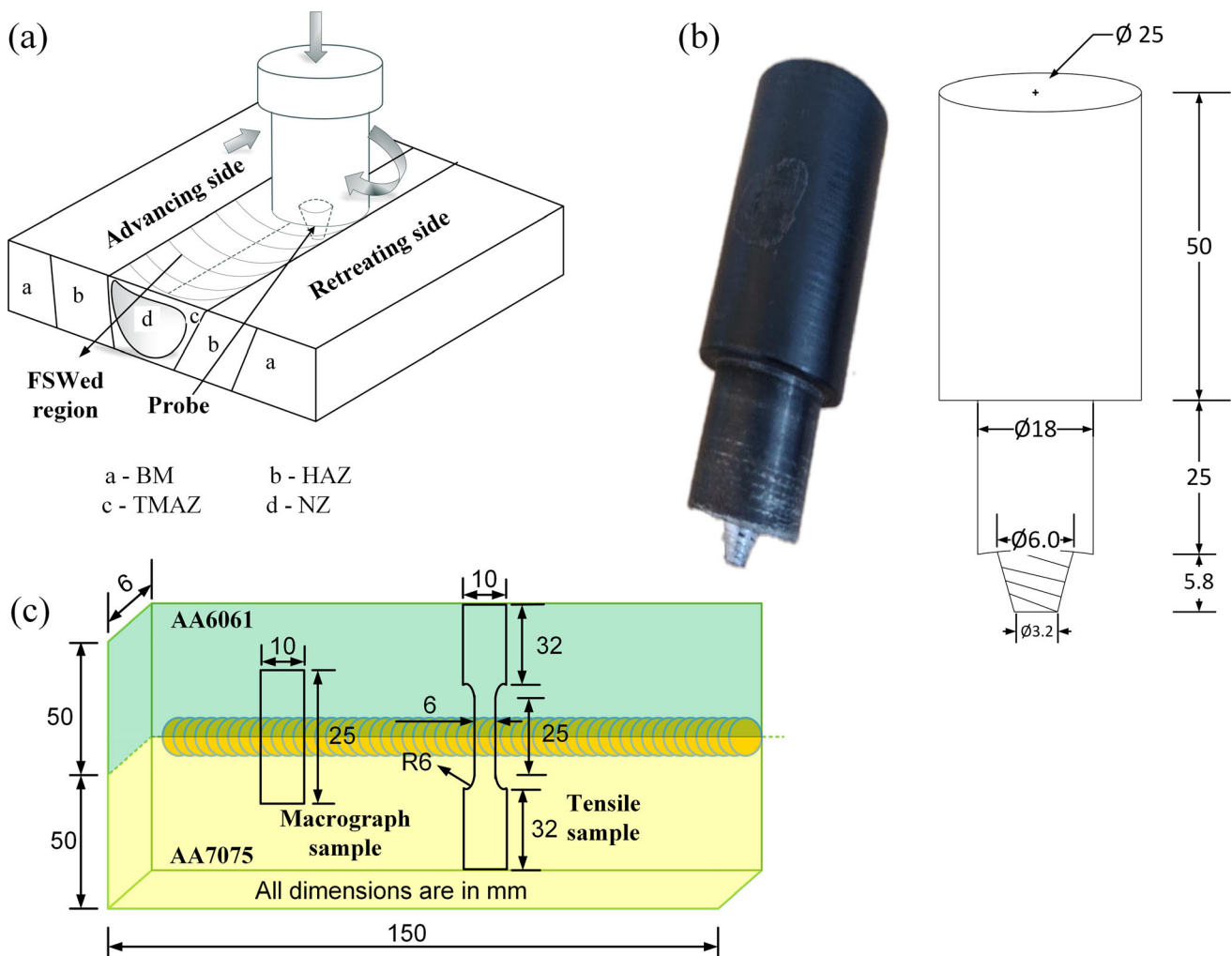


Fig. 1 Schematic diagrams of (a) FSW process, (b) Tool used for FSW process and (c) dimensions for tensile and macrograph specimen

Table 2 Process parameters used for the FSW method

Rotational rate, rpm	708	708	708	708
Traverse rate (mm/min)	20	30	40	60

Table 3 Tool dimensions used for the FSW method

Shoulder diameter	Probe diameter		Pin length
	Top	Bottom	
18	6	3.2	5.8

dissimilar AA6061/AA7075, such as grain orientation spread map, image quality with grain boundary distribution, misorientation angle distribution, kernel average misorientation and grain size distribution structure are examined by EBSD. Precipitation particles and elements of Al alloy are confirmed by FE-SEM with EDS analysis and area mapping, respectively. Transmission electron microscopy (TEM) is also employed to analyze the distribution of precipitation particles.

2. Experimental Procedure

AA7075-T6 and AA6061-T6 were used for the FSW process. Sample dimensions (150 mm × 50 mm × 6 mm) were employed for butt joint welding. The OES (optical

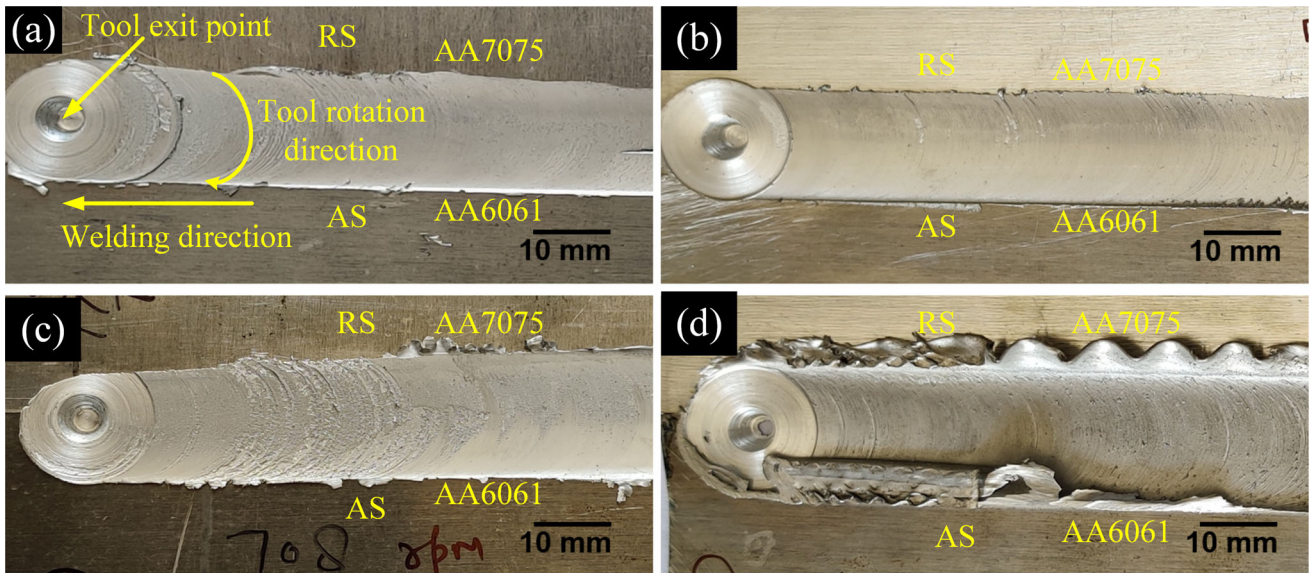


Fig. 2 Surfaces of the FSWed plates at various tool traverse rates (a) 20, (b) 30, (c) 40 and (d) 60 mm/min. (RS: Retreating side, AS: Advancing side)

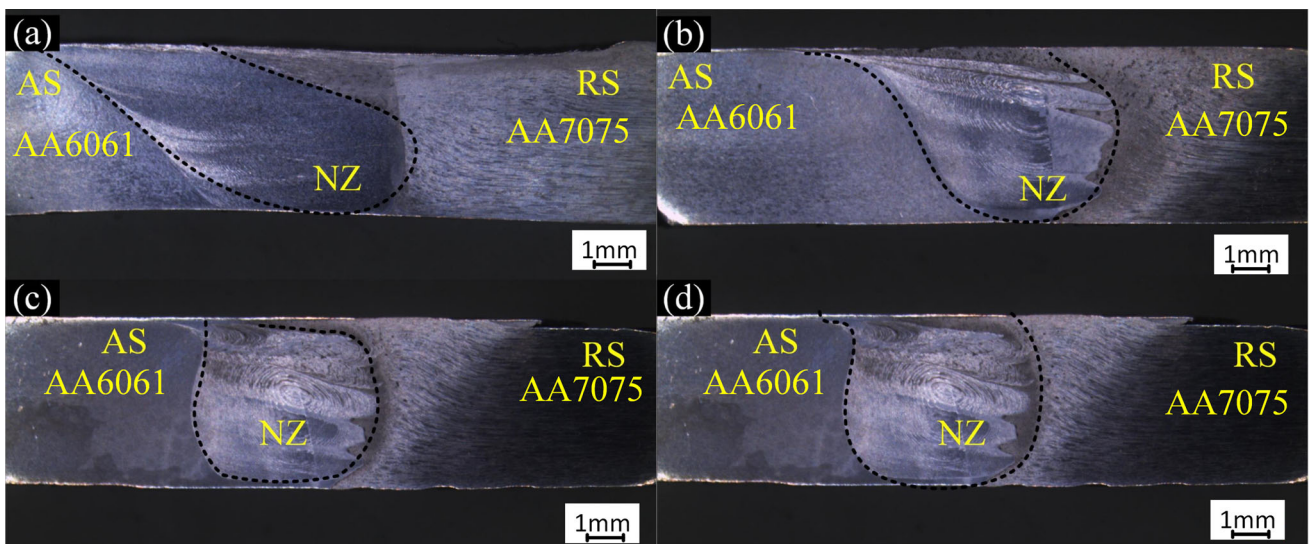


Fig. 3 Macrograph of dissimilar FSWed joint of AA7075 and AA6061 at various tool traverse rates (a) 20, (b) 30, (c) 40 and (d) 60 mm/min. (The retreating side, nugget zone and advancing side are labeled as RS, NZ, and AS respectively)

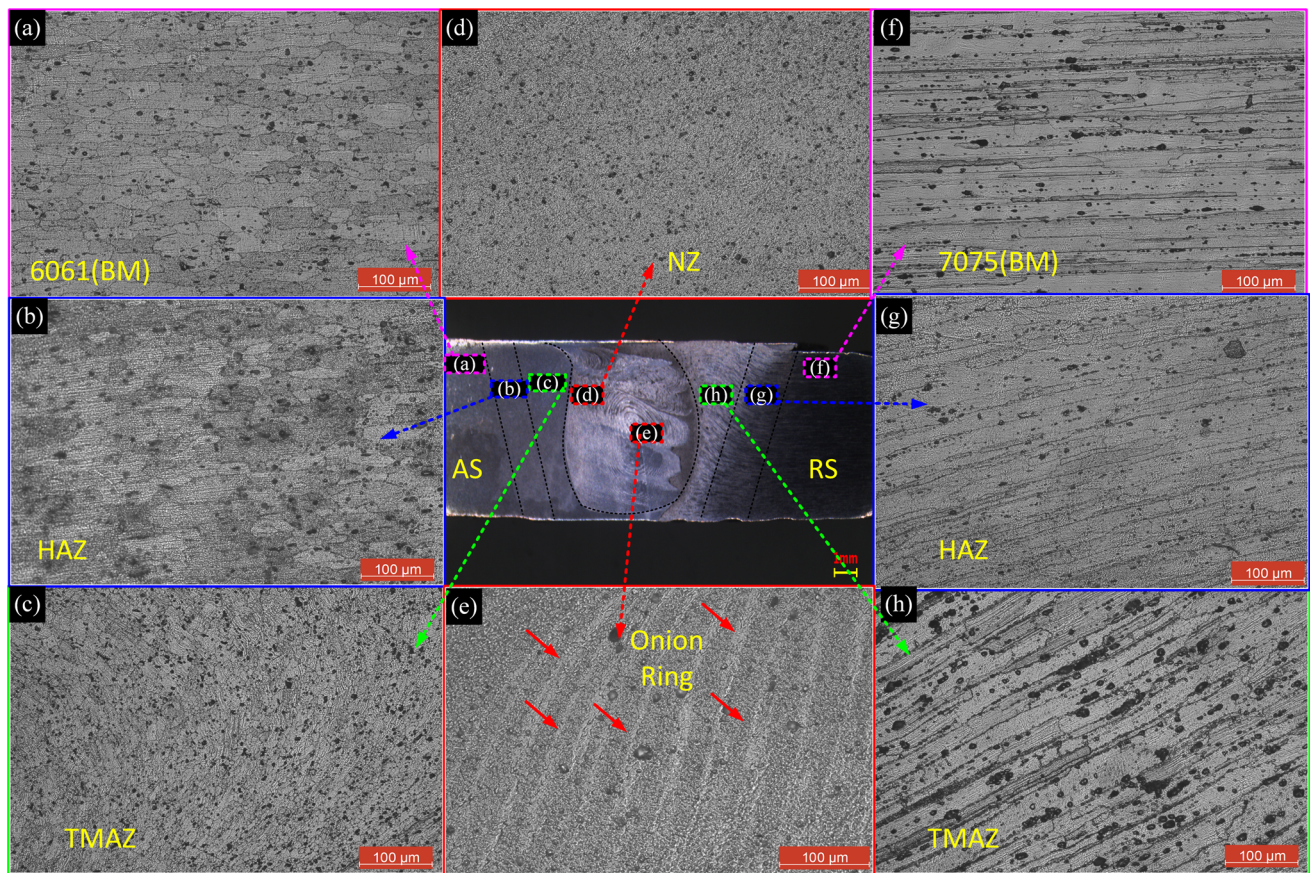


Fig. 4 Optical micrographs of the FSWed plates (a-c) BM, HAZ and TMAZ of AA6061 respectively, (d) NZ, (e) Onion ring, (f-h) BM, HAZ and TMAZ of AA7075 respectively

emission spectroscopy) spectrometry was used to examine the compositions of AA7075 and AA6061, which is shown in Table 1. Plate sample surfaces were appropriately cleaned with emery paper and then using acetone before the welding process.

A modified vertical milling machine was used for conducting FSW experiments. Fig. 1(a) shows the schematic diagram of the FSW process. Both plates of dissimilar Al alloys were adequately cleaned and fixed in the fixture prior to the FSW operation. A non-consumable cylindrically tapered thread rotating tool of 'H13 tool steel' was employed for the experiments, as depicted in Fig. 1(b). Macrograph and Tensile specimens were used for the test, as shown in Fig. 1(c). Tool traverse speed (welding speed) was varied, but rotational speed (708 rpm) and tilt angle (2°) was kept constant. Tables 2 and 3 indicates the process parameters and tool dimensions used for the FSW process.

The surface appearances of FSWed plates with different traverse rates, as shown in Fig. 2, were used for microstructural characterization and various tests. Welded samples were first ground and polished using SiC (320 to 2500 grit papers), then fine cloth polishing with MgO powder to obtain a mirror-like surface finish. Modified Keller's etchant (98 ml H_2O , 2.8 ml HNO_3 , 2.0 ml HF and 1.5 ml HCl) was used on the mirror-like

polished surface for (10-30 s) to expose the surface's microstructural features and grain boundary contrast.

Optical microscopy (model-Dewinter LT-23B) provided a detailed quantification of the micrograph. FESEM with EBSD (Electron Backscattered Diffraction) (Model-Zeiss) was used for the micro-level elemental analysis of the dissimilar welded joint. The selected locations were subjected to EBSD analysis with a $0.15 \mu m$ step size. The TSL-OIM software was utilized to perform post-processing on the EBSD-scanned data. Throughout the EBSD process, a mean angular deviation (MAD) below 0.3° was consistently maintained. Thin foils with a thickness of less than $90 \mu m$ were prepared for TEM analysis, followed by a twin jet electropolishing with ethanol and perchloric acid (9:1) solution at 4.5 V with a temperature ($-30^\circ C$). TEM analysis was used to quantify the precipitates embedded in the matrix and SAD (Selected Area Diffraction) patterns.

Further, a micro-hardness study of the dissimilar welded joint was carried out on Vickers's microhardness tester with dwell time, distance and load as 10 s, 0.5 mm and 100 g, respectively. Tensile specimens of the dissimilar welded joints were prepared with ASTM E-8 standard, and NZ was kept in the middle to measure the joint strength. Tensile tests were

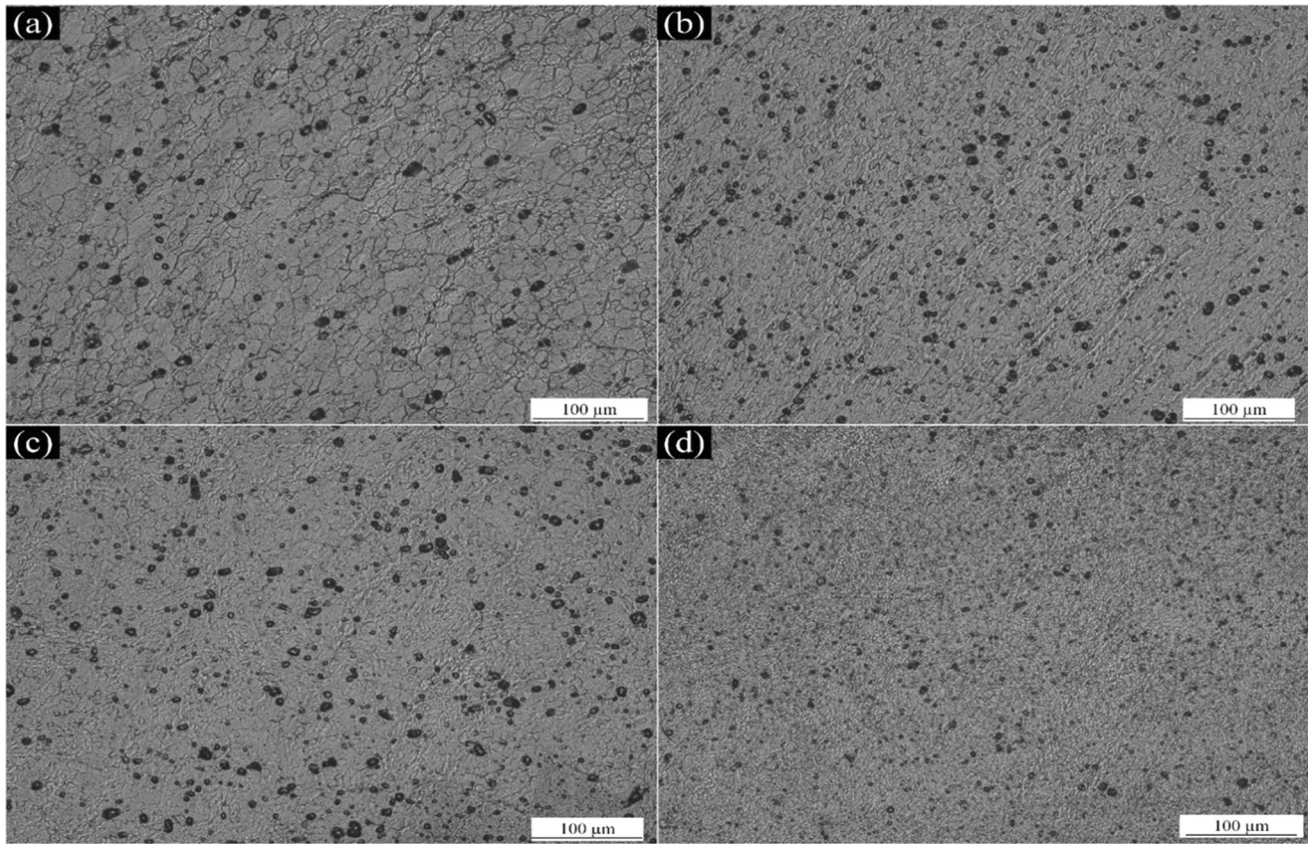


Fig. 5 Optical micrographs of the NZ at various tool traverse rates of (a) 20, (b) 30, (c) 40 and (d) 60 mm/min

conducted at room temperature on UTM (Model -Instron USA, M-5980) with 100 kN. During the test, cross-head speed was maintained at 0.5 mm/min, and four trials were run continuously for each sample. Furthermore, the formation of the fractured surface was examined by FE-SEM.

3. Results and Discussion

3.1 Macrostructure Analysis

The macrograph of the upper surfaces of the dissimilar FSWed joints at various parameters is depicted in Fig. 3. All the welds were found to be defect-free joints. They had a smooth surface with optimized process parameters used in the experiments. This indicates that all the selected parameters generated an adequate amount of heat.

However, no onion ring was seen at a traverse rate of 20 mm/min indicating insufficient mixing during the process, as seen in Fig. 3(a) (Ref 39). Material flow governs the creation of an onion ring. If the material is unable to flow around the tool for more than one revolution, it indicates inadequate material mixing, resulting in the elimination of onion ring formation. (Ref 40, 41). The AA7075 side shows a darker region, while the AA6061 side shows a lighter region due to

distinct etching reactions by modified Keller's reagent. Material mixing is substantially more efficient when weaker material (AA6061) is positioned on the advancing side (AS). When high-strength material (AA7075) was positioned on the AS, it was difficult for lower-strength material to penetrate NZ fully (Ref 37).

3.2 Microstructure Characterization

The microstructures of the dissimilar FSWed zone reveal different features in various regions, as evidenced in Fig. 4. Typically, in terms of microstructure, the FSWed joint can be categorized into four regions, namely BM, NZ, TMAZ, and HAZ (Ref 42). After welding, the microstructure of BM stays almost identical to its initial condition due to low temperature throughout the operation. Therefore both dissimilar BM comprised coarse and elongated grains, as observed in Fig. 4(a) and (f). In contrast, the HAZ region has no apparent plastic deformation. As a result of the welding heat cycle, the grains become coarser (Fig. 4b and g), which degrades the mechanical properties of joints. The TMAZ region exhibits coarser grains and moves upward to the tool, as seen in Fig. 4c and h. However, the materials in these locations undergo extensive plastic deformation as a result of extruding action from the NZ throughout the operation. No visual

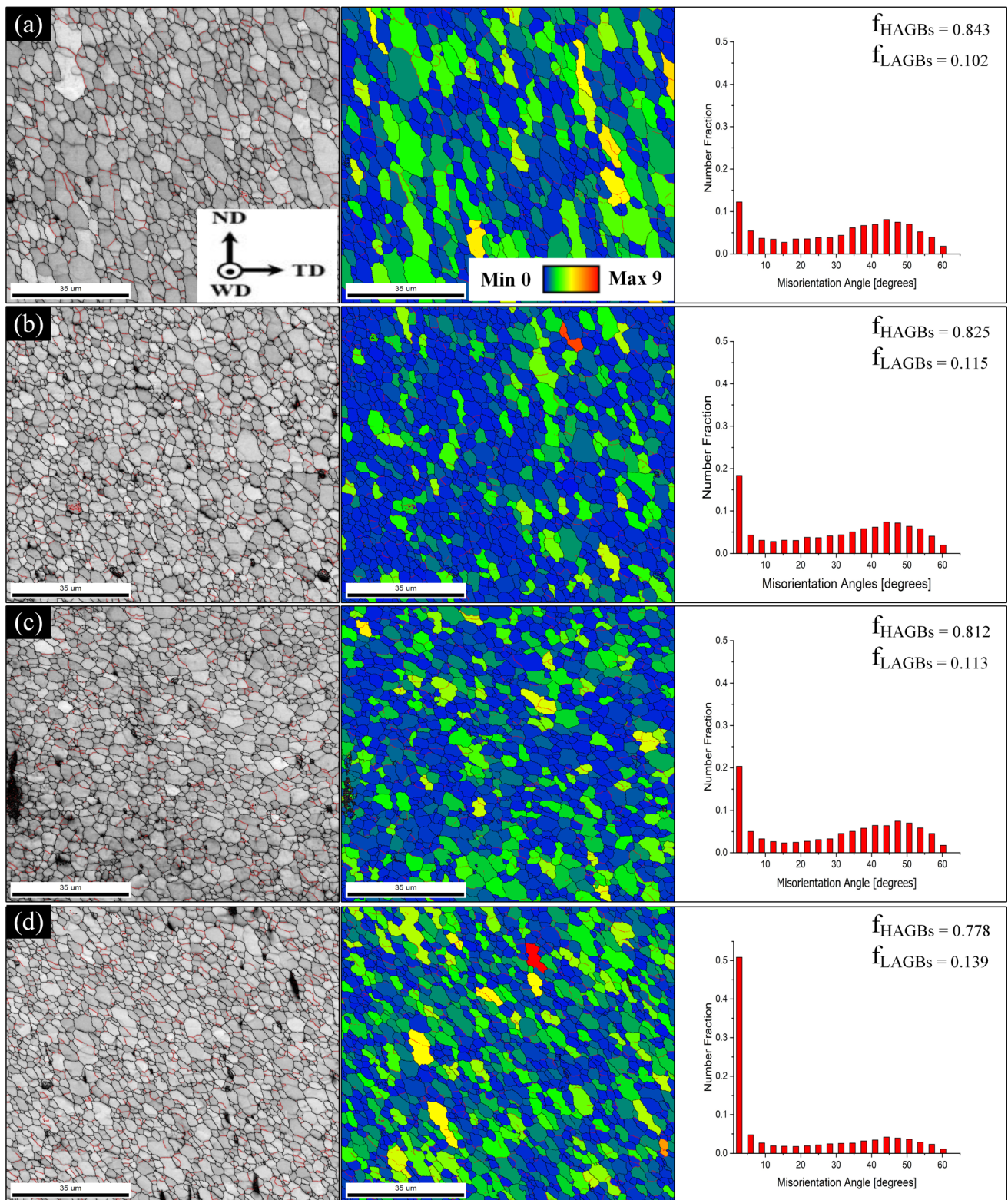


Fig. 6 Image quality map superimposed with grain boundaries (IQ + GB), Grain orientation spread (GOS) map and misorientation angle distribution histograms obtained from EBSD scan at traverse rates (a) 20, (b) 30, (c) 40 and (d) 60 mm/min, respectively

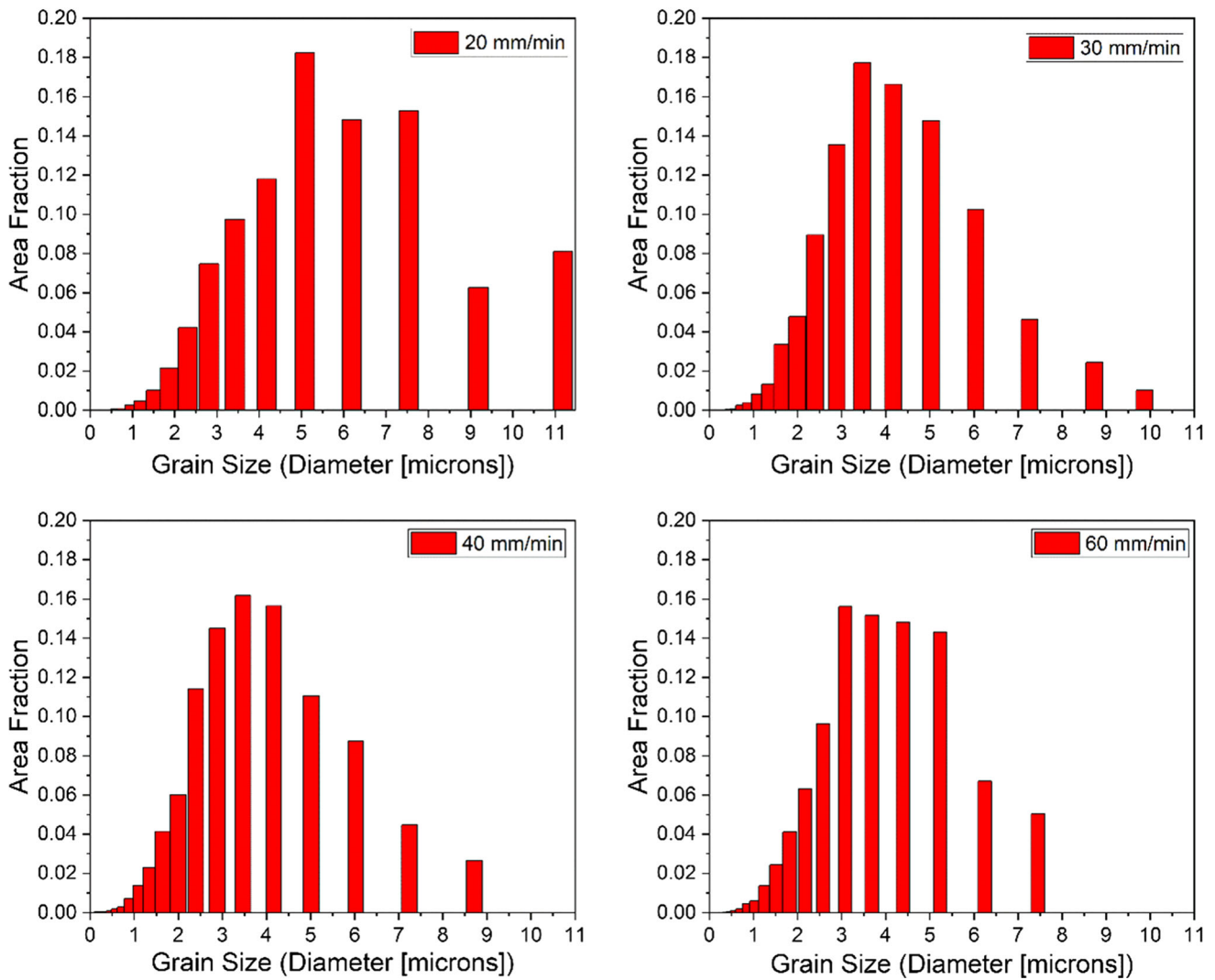


Fig. 7 Area fraction vs. Grain size distribution plot of NZ at traverse rates (a) 20, (b) 30, (c) 40 and (d) 60 mm/min, respectively

recrystallization appeared in this area. Fig. 4(d) shows that the NZ undergoes extensive grain refinement, distinguished by fine and equiaxed grains compared to other regions. These fine strain-free grains in NZ are a typical feature of dynamic recrystallization (DRX) induced by the combined impact of significant plastic deformation and intense frictional heat (Ref 43, 44). As red arrows indicate, Fig. 4e depicts the onion ring within NZ.

Fig. 5(a-d) shows the optical micrographs of NZ at various traverse rates. Fig. 5(a-d) indicates that the grain's size reduced steadily as the traverse rate increased from (20-60 mm/min). The average grain size was determined to be 5.82 μm (Fig. 5a) at a traverse rate of 20 mm/min. The smallest average grain was determined to be 3.64 μm at a traverse rate of 60 mm/min (Fig. 5d). The findings of the current research are well

consistent with those of the previous investigations (Ref 45-47). The grain size of the NZ of dissimilar FSWed joints was influenced by two thermomechanical factors, i.e., the amount of heat input and the amount of plastic deformation encountered throughout the process. The increment in tool traverse rate at a fixed rotating rate led to a decrement in the (heat input/length) throughout the process (Ref 48), which eventually restricted the coarsening of the grains owing to the reduction in heat input at a higher tool traverse rate.

EBSD analysis was carried out in the NZ region to extract the information related to grain and grain boundary characteristics, as depicted in Fig. 6. The various color contrast in the Grain Orientation Spread (GOS) maps are attributed to different crystallographic orientations of the grains. $\text{GOS} \leq 1^\circ$ has been used to calculate the dynamically recrystallized grain fraction.

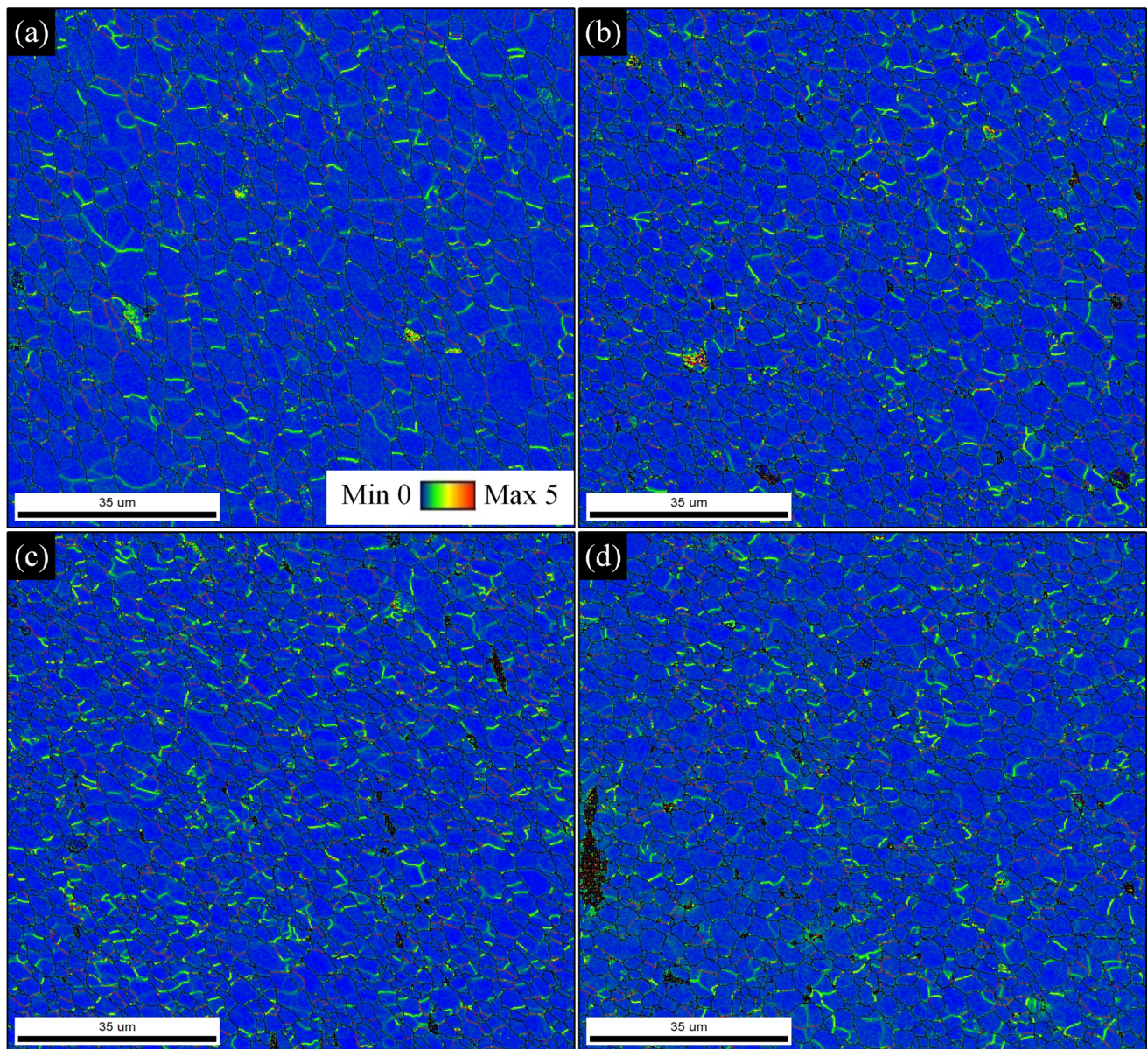


Fig. 8 The Kernel average misorientation (KAM) maps of NZ at traverse rates (a) 20, (b) 30, (c) 40 and (d) 60 mm/min, respectively

It can be observed that the percentage of recrystallized grains first increased from 0.8 to 0.87 pct with an increment of traverse rate from 20 to 30 mm/min. Furthermore, recrystallized grains decreased from 0.87 to 0.76 pct with an increased traverse rate from 30 to 60 mm/min. Fine grains were identified in NZ as a response to intense stirring and dynamic recrystallization. In the (IQ + GB) maps, the low-angle grain boundaries (LAGBs) are represented by red lines with a misorientation angle from 5° to 15° . In contrast, the high-angle grain boundaries (HAGBs) are shown by black lines with

greater than 15° misorientation angles. The percentages of LAGBs and HAGBs (in the NZ) were calculated using the cumulative probability distributions of the misorientation angles at $< 15^\circ$ and $> 15^\circ$, respectively.

According to the misorientation angle distributions, as seen in Fig. 6(a-d), the volume fraction of HAGBs marginally decreased in the NZ region with an increment of traverse rates. Besides, Fig. 7 depicts NZ's area fraction vs. grain size distribution plot at different traverse rates. The average grain sizes of the NZ were determined to be $5.827 \mu\text{m}$, $4.34 \mu\text{m}$,

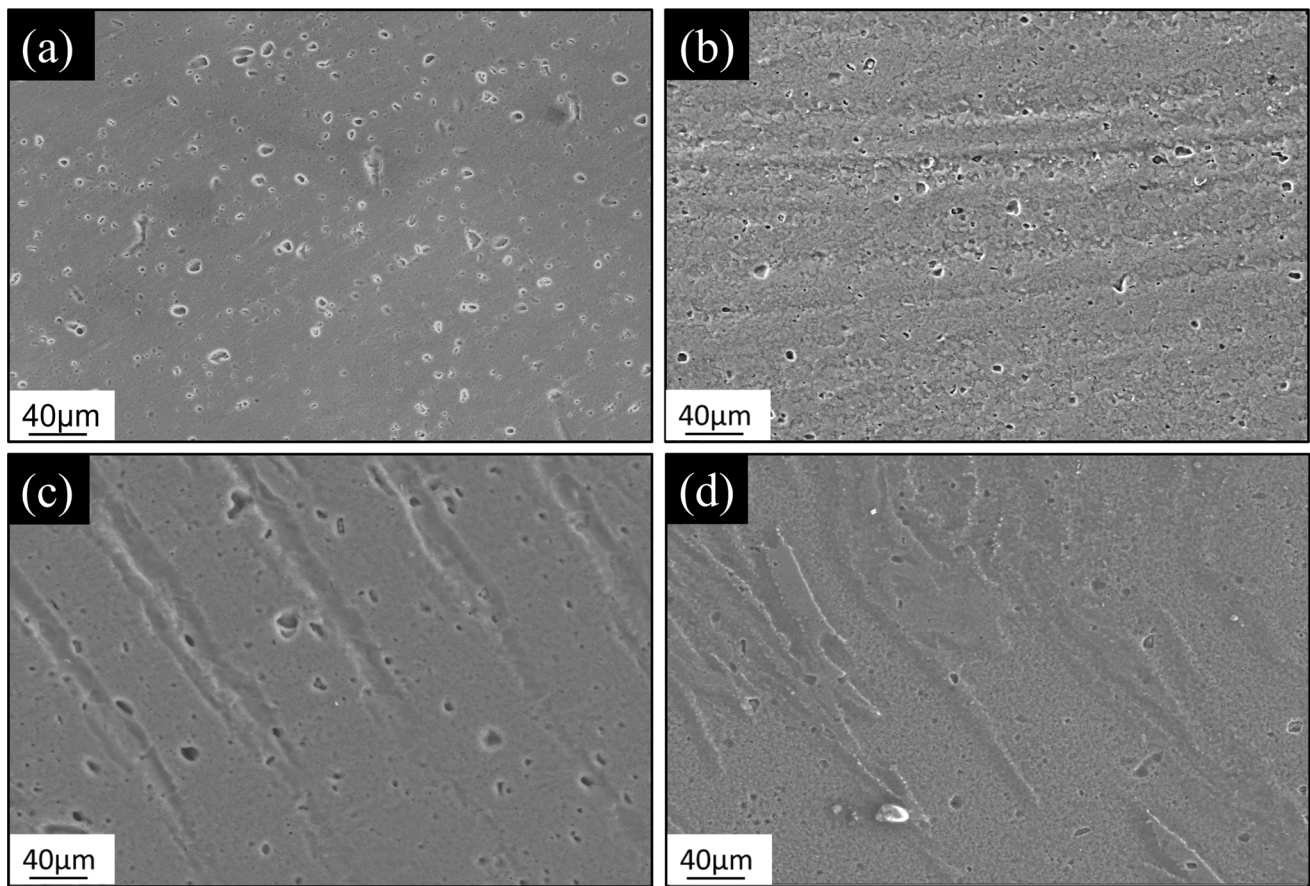


Fig. 9 Secondary electron images of the NZ at traverse rates (a) 20, (b) 30, (c) 40 and (d) 60 mm/min

3.94 μm and 3.64 μm at the traverse rates 20, 30, 40 and 60 mm/min, respectively. Variation in grain sizes between the dissimilar AA6061 and AA7075 Al alloys was insignificant. This occurrence is attributed to dynamic recrystallization, dynamic recovery (DRV), plastic deformation, material mixing and thermal cycle interaction throughout the process (Ref 49). Equiaxed, fine grains are seen in the NZ region because of the aforementioned factors. DRX is a phenomenon caused by heat input and plastic deformation that occur throughout the process (Ref 50, 51), which not only refines grains but also increases HAGBs (Ref 52). With the increment of traverse rate, sufficient DRX enhanced the grain refinement with a marginal decrement of HAGBs (Fig. 6a-d).

Kernel average misorientation KAM maps were generated from the EBSD scan to visualize the local plastic strain within the samples, as shown in Figure 8(a-d). The KAM value quantifies the average misorientation between neighboring orientation points and a specific central orientation point. The TSL-OIM software utilized the first nearest neighborhood to calculate the KAM map. To avoid any artificial influence from

adjacent grain boundaries, misorientations exceeding 5° were disregarded. The KAM value is often employed to describe dislocation density qualitatively. Moreover, the average local misorientation within a particular region indicates the presence of stored energy. The red and blue colored areas indicate the largest and lowest deformed areas and the KAM value, respectively. Most of the grains in the NZ of FSWed samples exhibit low KAM values (Fig. 8a-d), indicating strain-free grains. However, green patches overlie on the region with a moderate KAM value (containing grains with a medium dislocation density), suggesting the presence of dynamic recovery (DRV) (Ref 53).

Furthermore, the FSWed welded specimens processed at various traverse rates were investigated through an electron microscope to observe the creation of distinct zones, grains distribution, and intermixing of alloys. Fig. 9 shows the fine and equiaxed grain structure in NZ caused by stirring action and DRX on grains equivalent to a higher thermal cycle. The grain size in NZ is finer with an increased tool traverse rate. The onion ring patterns (Fig. 9b-d) signify the flow behavior and

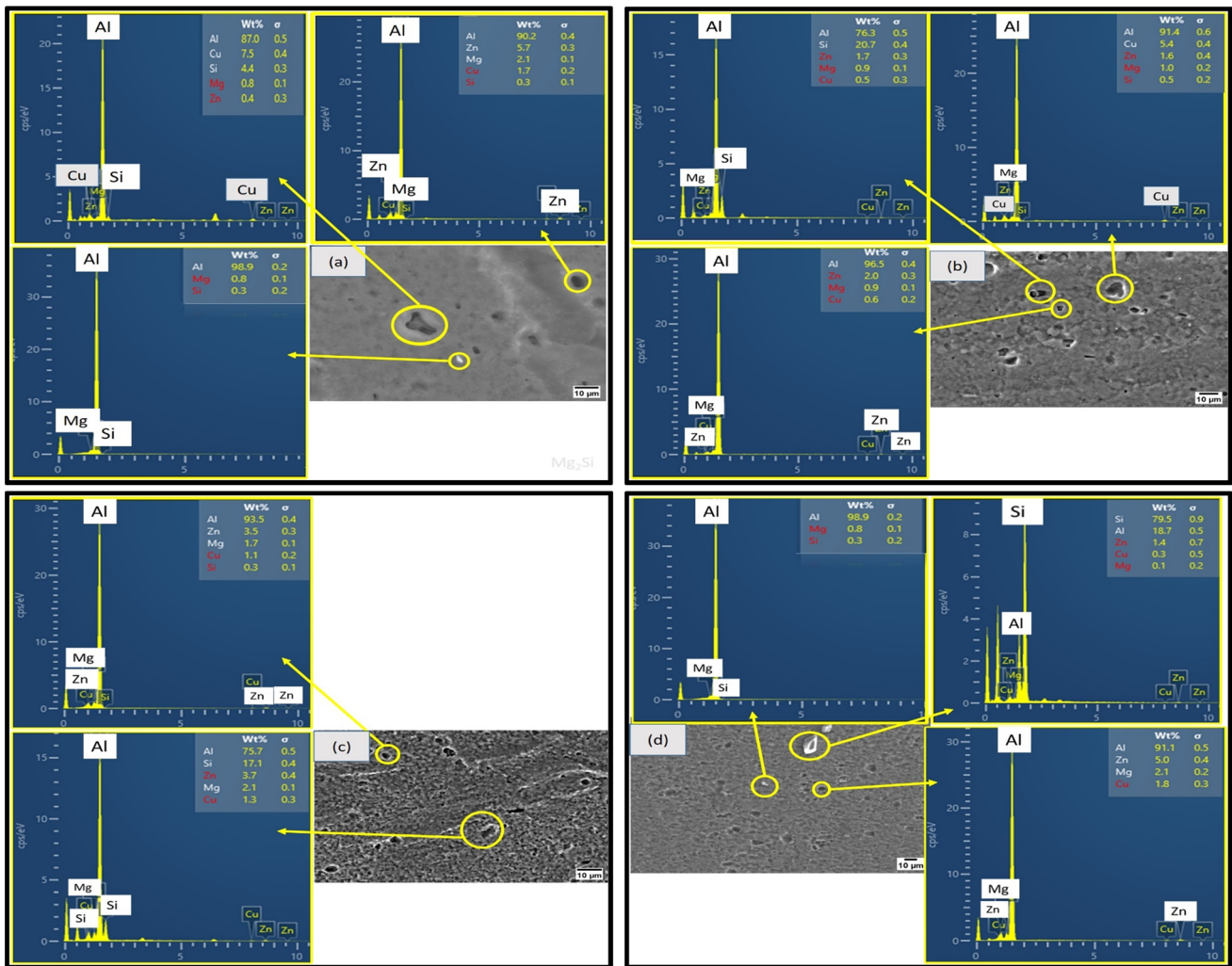


Fig. 10 EDS analysis of the precipitates in the NZ at traverse rates (a) 20, (b) 30, (c) 40 and (d) 60 mm/min

better mixing of both alloys in the NZ. Higher intermixing could enhance the joint's strength. Fig. 10 shows the magnified view of the FE-SEM image with EDS analysis of the NZ of the FSWed joints. EDS results indicate the presence of Mg_2Si , $MgZn_2$, and Al_2CuMg precipitates in the investigated zone (Fig. 10a-d). EDS area mapping is performed on the selected areas of the NZ with various tool traverse rates, as depicted in Fig. 11(a-d). The observation suggested that the distribution and mixing of Al, Zn, Mg, Cu and Si elements is relatively homogeneous.

TEM was used to study the property and morphology of the precipitates. For the current alloys, the precipitate evolution occurred in the following order:

For AA7075: SSS \rightarrow (GP) zones $\rightarrow \eta'$ $\rightarrow \eta$.

For AA6061: SSS \rightarrow (GP) zones $\rightarrow \beta''$ $\rightarrow \beta'$ $\rightarrow \beta$.

GP zones are solute-rich clusters of atoms in a particular plane that are very small and coherent to the matrix. The shape and size of GP zones can change with temperature and time changes. In AA7075 alloy, GP zones are spherical initially and then converted to plate shape in $\{111\}$ plane. The strengthening precipitates are well recognized as η' and the grain boundary η precipitates. The η' precipitate (~ 10 -50 nm) is semi-coherent to the matrix and plate-like shape, while incoherent stable η - $MgZn_2$ (more than 100 nm) exhibits both plate-like and lath-type morphology (Ref 19). On the other hand, in AA6061 alloy, a significant strengthening precipitate is a fine needle-shaped

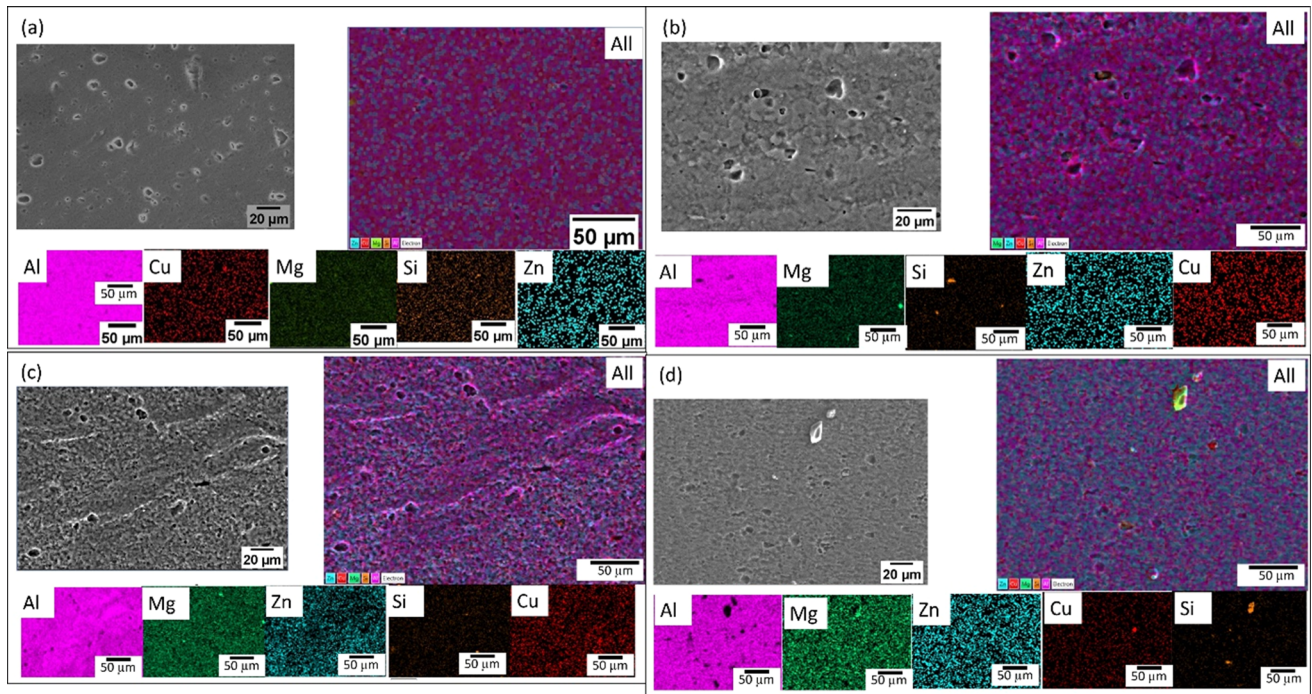


Fig. 11 FE-SEM images with EDS mapping of the NZ at traverse rates (a) 20, (b) 30, (c) 40 and (d) 60 mm/min

β'' . However, the softening mechanism occurred throughout the process due to localized heating eventually dissolving the β'' precipitates, and the re-precipitation of β' and equilibrium β - Mg_2Si precipitates occurs in NZ.

Figure 12 shows the TEM images of the NZ processed at various tool traverse rates. Red arrows indicate several precipitates in the NZ of the dissimilar FSWed joint. The result indicates the strengthening precipitates in the NZ region were dissolved while the η' , β' , η and β precipitates remained in the matrix. Previous literature illustrated that the NZ of AA6061 side shows different sizes and morphologies of rod shape β' precipitates, Si-enriched round precipitates and β phases. In contrast, the NZ of the AA7075 side shows GP zones, round type η' and rod shape η precipitates (Ref 54, 55). The re-precipitation may cause an increment in microhardness in the NZ region, followed by natural aging. Although, the

selected area diffraction pattern (SADP) (Fig. 13) along the zone axis suggests a corresponding plane of precipitates in the matrix.

3.3 Microhardness

The Vickers's microhardness of the FSWed samples was assessed from BM to the NZ for the dissimilar alloys used in the present study. FSWed joints exhibit lower micro-hardness in the NZ compared to the AA7075 BM region, as shown in Fig. 14. However, an opposite trend has been observed concerning the AA6061 BM region. Previous studies show that due to the coarsening, dissolution, and insufficient re-precipitation caused by the FSW thermal cycle, the hardness decreased in NZ compared to the BM for similar alloys (Ref 35). However, grain refinement could potentially provide some minor contributions to the increase of hardness in the BM. The

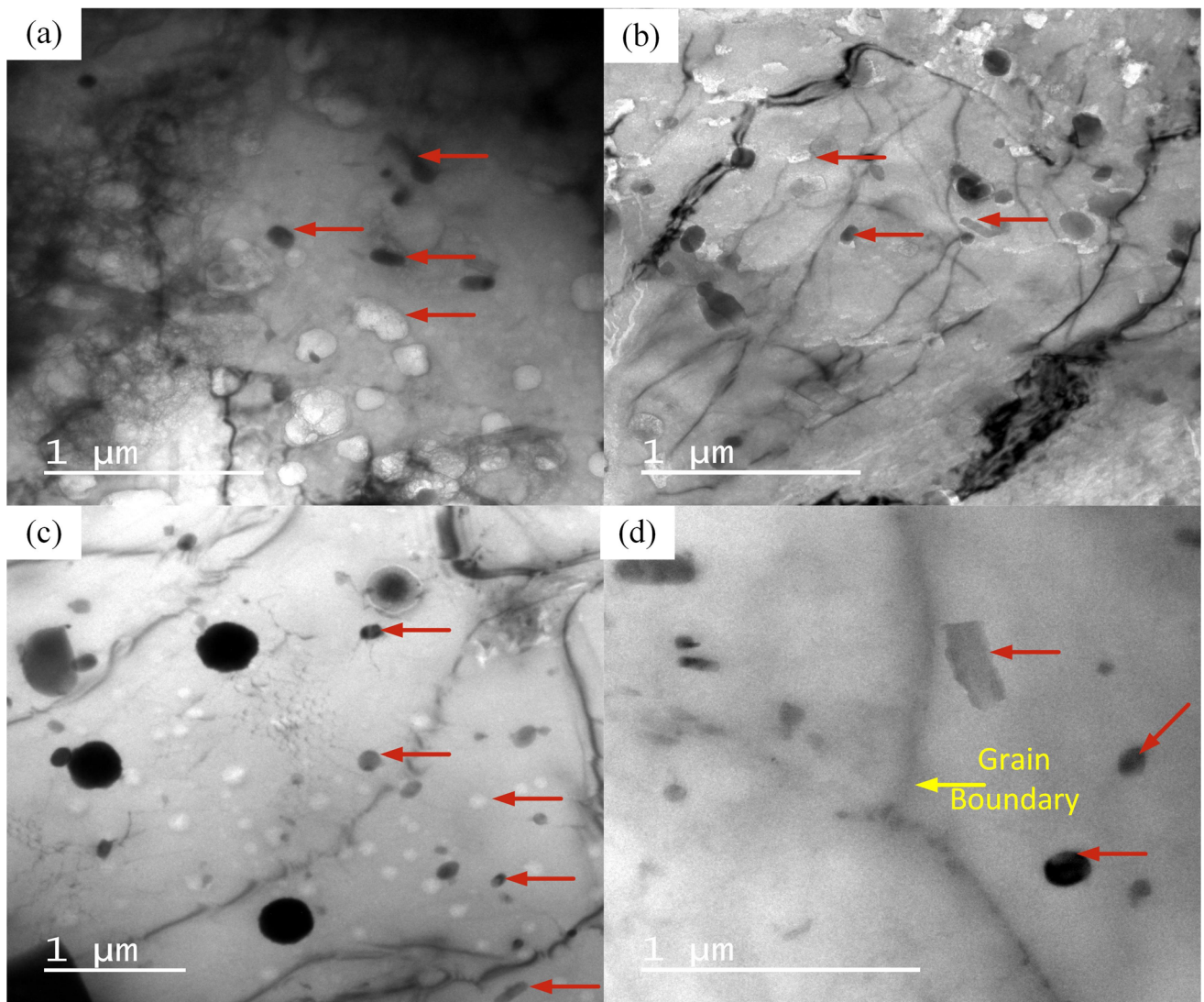


Fig. 12 TEM images of precipitates in the NZ region at traverse rates (a) 20, (b) 30, (c) 40, and (d) 60 mm/min

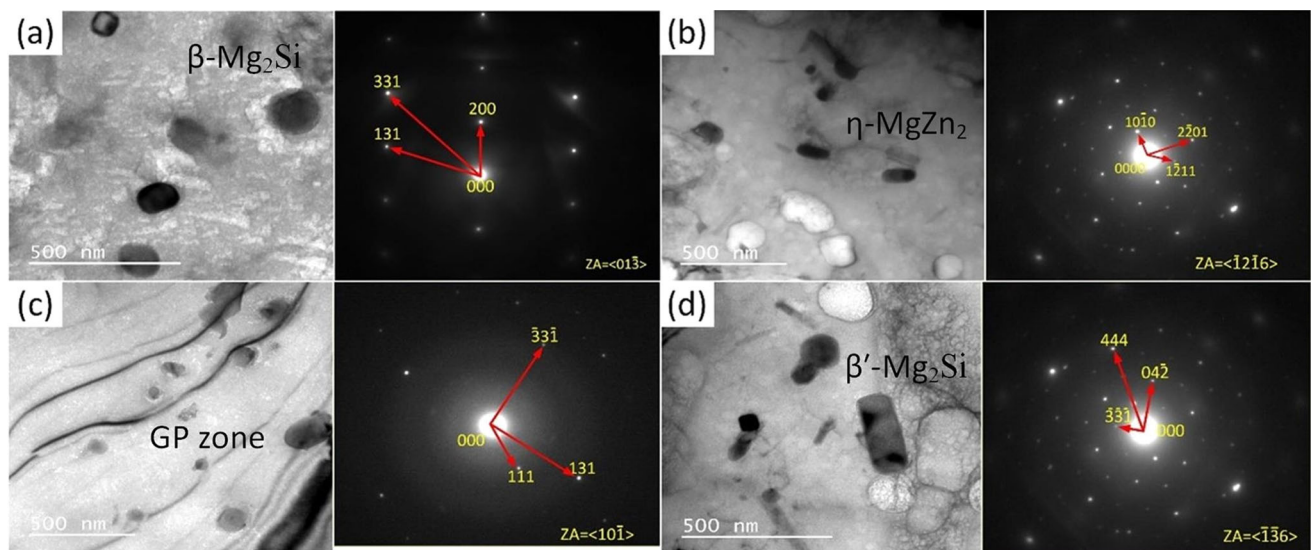


Fig. 13 TEM images of precipitates with corresponding SAD patterns in the NZ of the dissimilar FSWed plates at traverse rates (a) 20, (b) 30, (c) 40 and (d) 60 mm/min

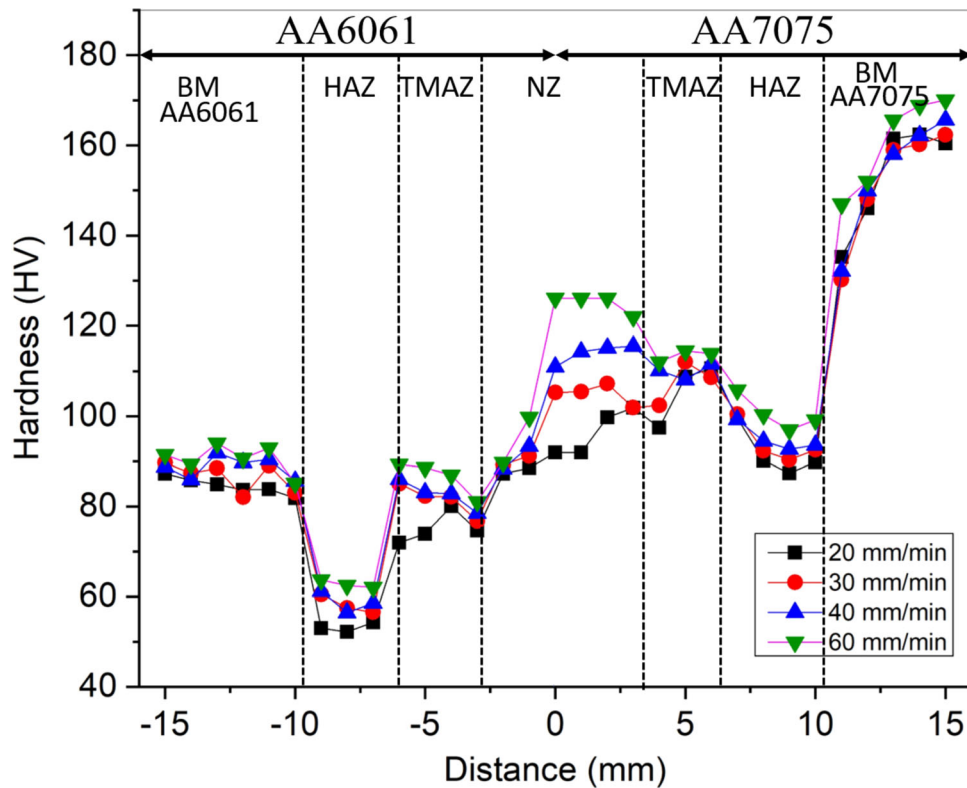


Fig. 14 Vickers micro-hardness distribution of dissimilar FSWed samples of AA6061 and AA7075

Table 4 Mechanical properties of FSWed joint of dissimilar AA6061 /AA7075

Traverse rates, mm/min	YS, MPa	UTS, MPa	TE, (%)	Joint efficiency, (%)	Failure position
20	96 ± 7	159 ± 3	8 ± 5	51	HAZ_6061
30	109 ± 3	167 ± 9	6 ± 5	54	HAZ_6061
40	141 ± 6	237 ± 4	5 ± 6	76	HAZ_6061
60	150 ± 8	251 ± 6	8 ± 2	81	HAZ_6061

disappearance of GP zones and coarsening of precipitates causes the lowest hardness in the HAZ region. In the TMAZ region, precipitates underwent more significant coarsening and probably full dissolution. Material suffered some re-precipitation in the NZ region after complete dissolution due to higher temperature. Micro-hardness transition in NZ is more gradual when AA6061 is kept on the AS. This indicates an efficient mixing of materials under these conditions.

3.4 Mechanical Properties

Table 4. depicts the mechanical properties of the FSWed joints of dissimilar AA6061/AA7075. Fig. 15 depicts the tensile specimen macrographs before testing and after testing, along with stress-strain curves. The macrograph of the broken tensile specimen showed that all the joints have failed at the

location of HAZ of AA6061 side, where the minimal hardness is found (Fig. 15c). Previous studies show that the FSWed joints generally fracture at the HAZ region on the weaker material side (Ref 56-58).

All the FSWed joints exhibited superior tensile properties with a yield strength (YS), ultimate tensile strength (UTS) and elongation of around 5-8%. The UTS was recorded to be 159, 167, 237 and 251 MPa with tool traverse rates of 20, 30, 40 and 60 mm/min, respectively, showing gradual increments with the increase in traverse rate. The best combination of strength and ductility was achieved at a traverse rate of 60 mm/min, as shown in Table 4. Variation in the tensile values of these joints correlates with the microstructural features discussed in the relevant sections. The increase in the traverse rate reduces heat input, which eventually hinders grain growth and precipitates coarsening, restricting the deterioration of HAZ strength.

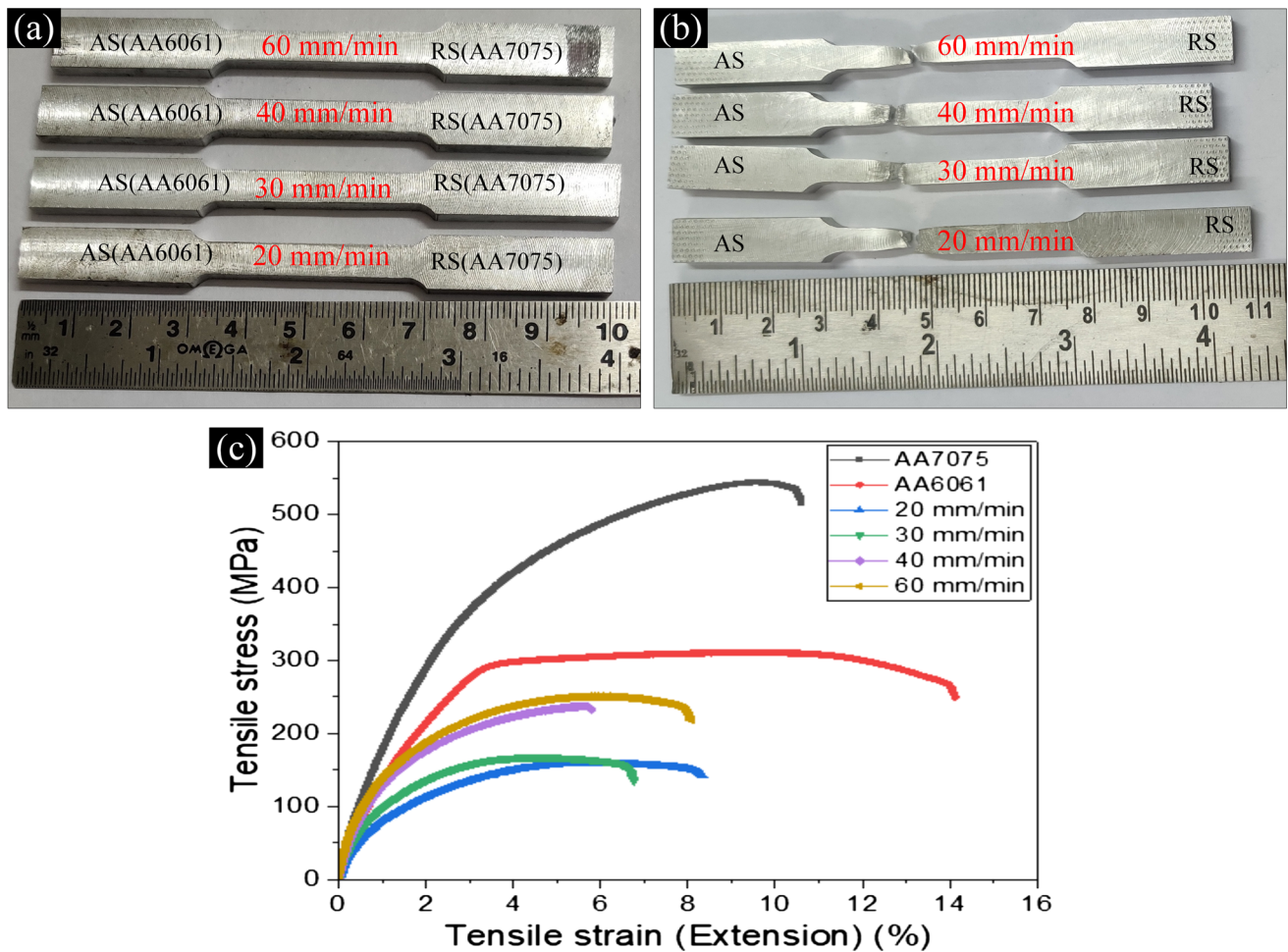


Fig. 15 (a) Macrograph of the tensile specimen before testing, (b) macrograph of a broken tensile specimen, (c) tensile curves (stress vs. strain) of the investigated samples

Therefore, the FSWed joint fabricated by a higher tool traverse rate exhibited superior mechanical properties, as seen in the present study (Fig. 15b).

3.5 Fractographic Analysis

The primary fracture planes of the broken tensile samples have been examined under FE-SEM to dig out more insights into the nature of the fracture mechanism. The fracture surfaces of all the samples show a shear type of deformation with the formation of micro-voids predominantly, as a typical ductile fracture, as shown in Fig. 16.

The presence of several dimples and micro-voids suggests a ductile fracture with excellent joint strength. Shallow dimples of different sizes are illustrated in Fig. 16(a). Additionally, Fig. 16b-c and d display small, equiaxed dimples resulting from micro-void coalescence due to increased strain during tensile testing. The micro-voids may form around second-phase particles, inclusions, and dislocation pileups. As a result, the equiaxed and fine dimples are formed probably at a traverse

rate of 60 mm/min during the FSW process. Fig. 17(a-d) shows the evidence of the β -Mg₂Si phase at the HAZ region on AA6061 alloys.

4. Conclusions

In the current study, dissimilar AA7075 /AA6061 were welded by the FSW method. The welding process was performed at a constant rotation rate of 708 rpm, accompanied by traverse rates of 20, 30, 40, and 60 mm/min. The following findings were obtained after investigating the microstructure and mechanical characteristics:

1. All the FSWed joints were defect-free and exhibited excellent surface weld appearance with the combination of parameters.
2. Dissimilar AA7075/AA6061 FSWed joints experienced dynamic recrystallization (DRX), indicated by fine and

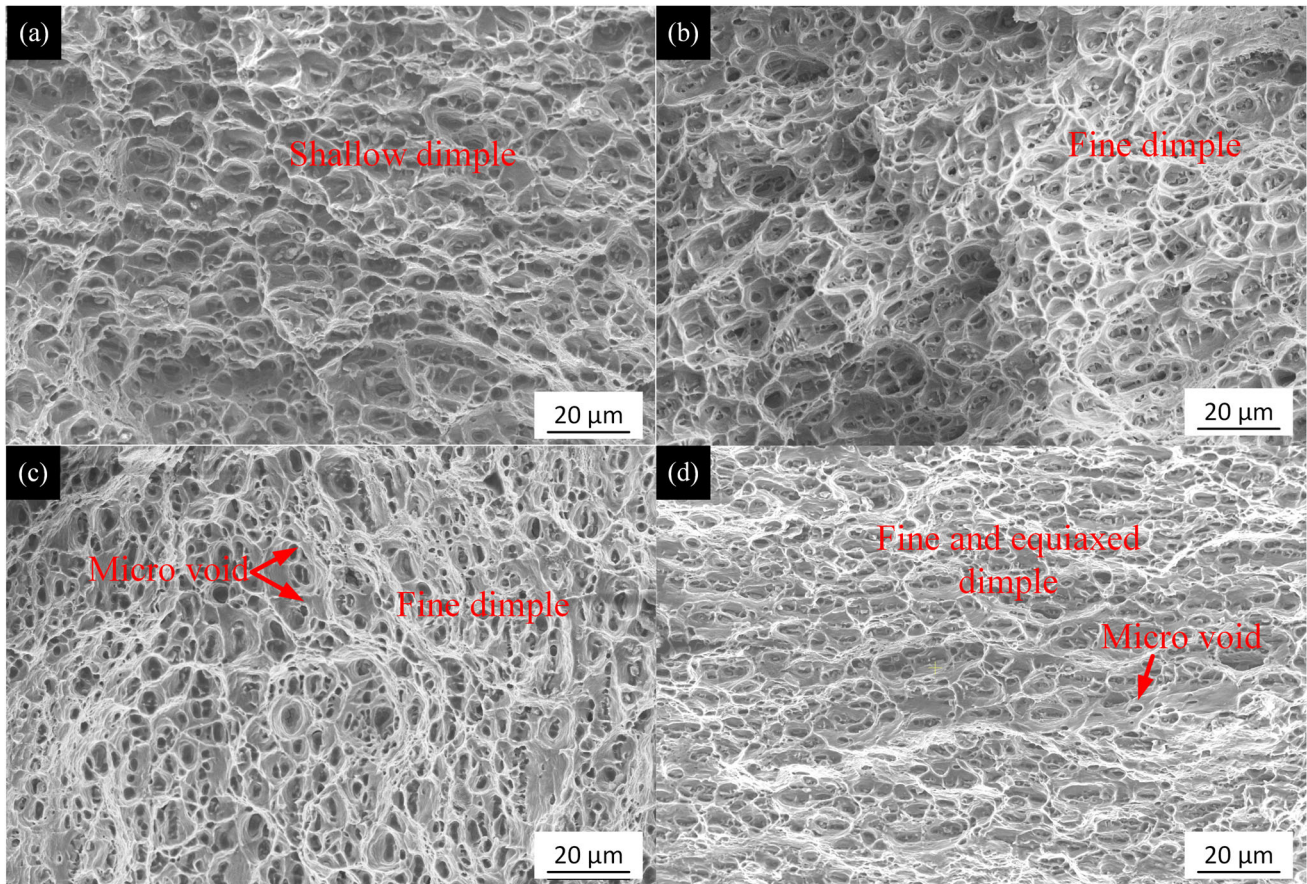


Fig. 16 Fractography analysis of the tensile tested FSWed samples at traverse rates (a) 20, (b) 30, (c) 40 and (d) 60 mm/min

equiaxed grains in the NZ. This enables sound welds with superior mechanical properties. The average grain sizes in the NZ were determined to be $5.82 \mu\text{m}$, $4.34 \mu\text{m}$, $3.94 \mu\text{m}$, and $3.64 \mu\text{m}$ at tool traverse rates of 20, 30, 40, and 60 mm/min, respectively.

3. Compared to their equivalent BM, both AA7075 and AA6061 showed a reduction in microhardness in the NZ region. The coarsening and dissolution of the strengthening precipitation cause softening in NZ. Furthermore, re-precipitated during natural aging resulted in an increase in microhardness in NZ. The AA6061 side of the HAZ exhibited the lowest hardness (condition of 20 mm/min traverse rate).
4. All the tensile specimens broke at the position of HAZ (AA6061 side), where minimal hardness was found and

showed descent UTS, YS and ductility. UTS and YS increased with the increment of traverse rate from 20 to 60 mm/min. The UTS was obtained at 251 MPa at a traverse rate (60 mm/min). In contrast, the minimum UTS was obtained as 159 MPa for the constant rotational rate (708 rpm) and traverse rate (20 mm/min).

5. Many fine dimples of varying sizes distinguished the fractured surfaces of tensile investigated specimens. Under lesser heat input, the cracked surfaces of the joints produced fine and equiaxed dimples. During fracture, second-phase particles such as incoherent Mg_2Si and different Al-Fe-Si intermetallics may efficiently supply microvoid nucleation sites, as confirmed by the eds analysis under FE-SEM.

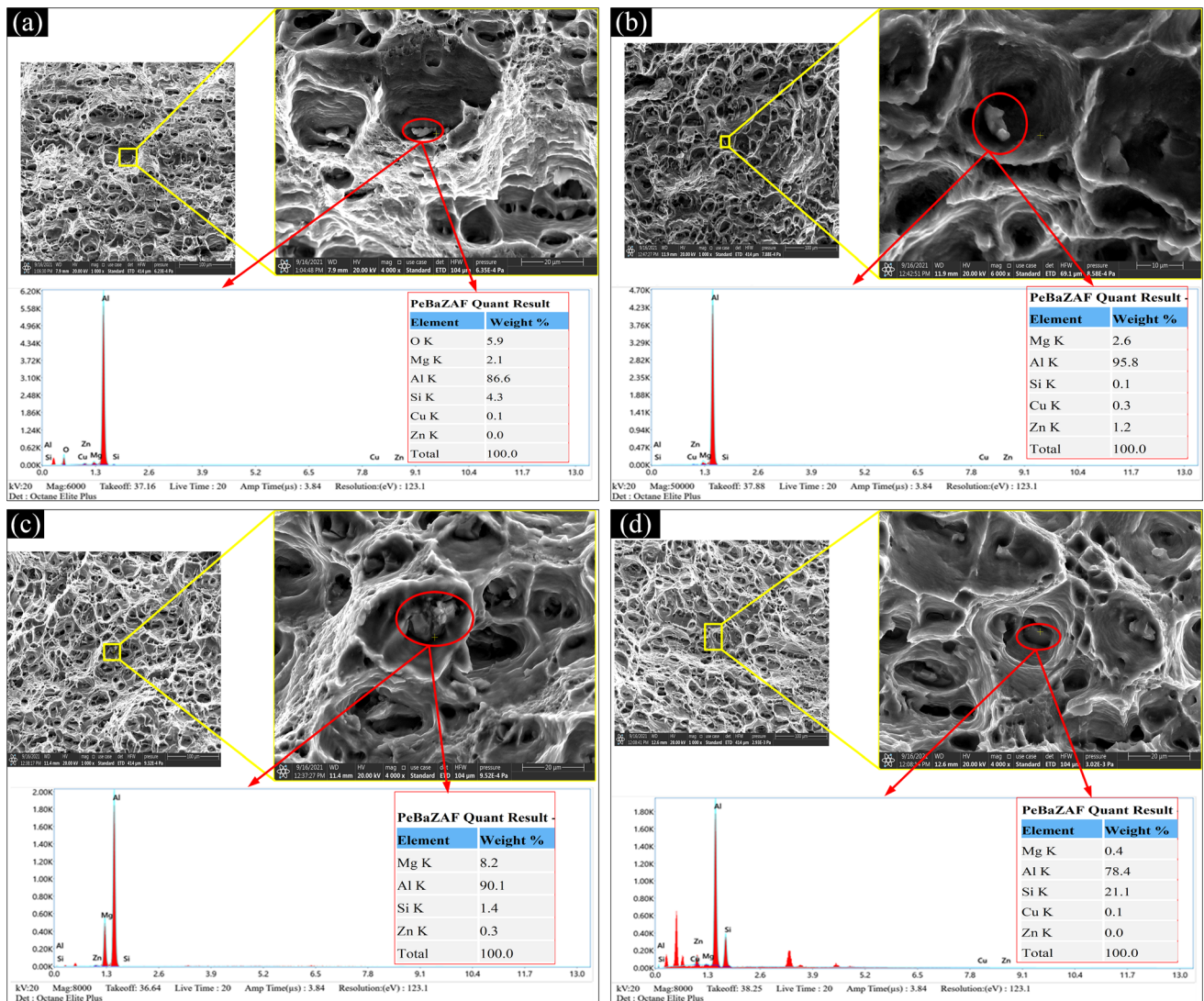


Fig. 17 EDS analysis of the tensile tested FSWed samples at traverse rates (a) 20, (b) 30, (c) 40 and (d) 60 mm/min

Acknowledgements

The authors are highly grateful for the Institute Assistantship IIT Roorkee offered to the first author to carry out the present work.

Competing interest

The authors declare that they have no known competing financial interests or personal relationships that could have appeared to influence the work reported in this paper.

References

- W.S. Miller, L. Zhuang, J. Bottema, A.J. Wittebrood, P. De Smet, A. Haszler and A. Viererger, Recent Development in Aluminium Alloys for the Automotive Industry, *Mater. Sci. Eng. A*, 2000, **280**(1), p 37–49.
- X. Peng, Q. Guo, X. Liang, Y. Deng, Y. Gu, G. Xu and Z. Yin, Mechanical Properties, Corrosion Behavior and Microstructures of a Non-Isothermal Ageing Treated Al-Zn-Mg-Cu Alloy, *Mater. Sci. Eng. A*, 2016, **2017**(688), p 146–154.
- E. Sharghi and A. Farzadi, Simulation of Strain Rate, Material Flow, and Nugget Shape during Dissimilar Friction Stir Welding of AA6061 Aluminum Alloy and Al-Mg₂Si Composite, *J. Alloys Compd.*, 2018, **748**, p 953–960. <https://doi.org/10.1016/j.jallcom.2018.03.145>
- H.C. Fang, H. Chao and K.H. Chen, Effect of Zr, Er and Cr Additions on Microstructures and Properties of Al-Zn-Mg-Cu Alloys, *Mater. Sci. Eng. A*, 2014, **610**, p 10–16. <https://doi.org/10.1016/j.msea.2014.05.021>
- R. Saravanakumar, T. Rajasekaran and C. Pandey, Underwater Friction Stir Welded Armour Grade AA5083 Aluminum Alloys: Experimental Ballistic Performance and Corrosion Investigation, *J. Mater. Eng. Perform.*, 2023 <https://doi.org/10.1007/s11665-023-07836-2>
- F.F. Wang, W.Y. Li, J. Shen, S.Y. Hu and J.F. dos Santos, Effect of Tool Rotational Speed on the Microstructure and Mechanical Properties of Bobbin Tool Friction Stir Welding of Al-Li Alloy, *Mater. Des.*, 2015, **86**, p 933–940.
- K. Singh, G. Singh and H. Singh, Review on Friction Stir Welding of Magnesium Alloys, *J. Magnes. Alloy.*, 2018, **6**(4), p 399–416. <https://doi.org/10.1016/j.jma.2018.06.001>
- N.Z. Khan, A.N. Siddiquee, Z.A. Khan and A.K. Mukhopadhyay, Mechanical and Microstructural Behavior of Friction Stir Welded Similar and Dissimilar Sheets of AA2219 and AA7475 Aluminium Alloys, *J. Alloys Compd.*, 2017, **695**, p 2902–2908. <https://doi.org/10.1016/j.jallcom.2016.11.389>
- J.A.N.G. Jae-Ho, N.A.M. Dae-Geun, P.A.R.K. Yong-Ho and P.A.R.K. Ik-Min, Effect of Solution Treatment and Artificial Aging on Microstructure and Mechanical Properties of Al-Cu Alloy, *Trans.*

- Nonferrous Met. Soc. China*, 2013, **23**(3), p 631–635. [https://doi.org/10.1016/S1003-6326\(13\)62509-1](https://doi.org/10.1016/S1003-6326(13)62509-1)
10. K.A. Zakaria, S. Abdullah and M.J. Ghazali, Comparative Study of Fatigue Life Behaviour of AA6061 and AA7075 Alloys under Spectrum Loadings, *Mater. Des.*, 2013, **49**(48), p 57. <https://doi.org/10.1016/j.matdes.2013.01.020>
 11. R. Beygi, H. Pouraliakbar, K. Torabi, V. Fallah, S.K. Kim, R. Shi and L.F.M. da Silva, The Inhibitory Effect of Stir Zone Liquefaction and Eutectic-Phase Formation on the Growth of γ/β Intermetallics during Dissimilar FSW of Al/Mg Alloys, *J. Manuf. Process.*, 2021, **70**, p 152–162. <https://doi.org/10.1016/j.jmapro.2021.08.049>
 12. J.R. Pickens, Aluminium Powder Metallurgy Technology for High-Strength Applications, *J. Mater. Sci.*, 1981, **16**(6), p 1437–1457.
 13. T. Gao, Y. Zhang and X. Liu, Influence of Trace Ti on the Microstructure, Age Hardening Behavior and Mechanical Properties of an Al-Zn-Mg-Cu-Zr Alloy, *Mater. Sci. Eng. A*, 2014, **598**, p 293–298. <https://doi.org/10.1016/j.msea.2014.01.062>
 14. T. Marlaud, B. Malki, C. Henon, A. Deschamps and B. Baroux, Relationship between Alloy Composition, Microstructure and Exfoliation Corrosion in Al-Zn-Mg-Cu Alloys, *Corros. Sci.*, 2011, **53**(10), p 3139–3149. <https://doi.org/10.1016/j.corsci.2011.05.057>
 15. T. Dursun and C. Soutis, Recent Developments in Advanced Aircraft Aluminium Alloys, *Mater. Des.*, 2014, **56**, p 862–871. <https://doi.org/10.1016/j.matdes.2013.12.002>
 16. K. El-Menshawey, A.W.A. El-Sayed, M.E. El-Bedawy, H.A. Ahmed and S.M. El-Raghy, Effect of Aging Time at Low Aging Temperatures on the Corrosion of Aluminum Alloy 6061, *Corros. Sci.*, 2012, **54**(1), p 167–173. <https://doi.org/10.1016/j.corsci.2011.09.011>
 17. M.K. Hagnell, S. Kumaraswamy, T. Nyman and M. Akermo, From Aviation to Automotive: A Study on Material Selection and Its Implication on Cost and Weight Efficient Structural Composite and Sandwich Designs, *Heliyon*, 2020, **6**(3), p e03716. <https://doi.org/10.1016/j.heliyon.2020.e03716>
 18. M. Paidar, R.V. Vignesh, A. Moharrami, O.O. Ojo, A. Jafari and S. Sadreddini, Development and Characterization of Dissimilar Joint between AA2024-T3 and AA6061-T6 by Modified Friction Stir Clinching Process, *Vacuum*, 2020, **176**, p 109298. <https://doi.org/10.1016/j.vacuum.2020.109298>
 19. T.F. Chung, Y.L. Yang, M. Shiojiri, C.N. Hsiao, W.C. Li, C.S. Tsao, Z. Shi, J. Lin and J.R. Yang, An Atomic Scale Structural Investigation of Nanometre-Sized η Precipitates in the 7050 Aluminium Alloy, *Acta Mater.*, 2019, **174**, p 351–368. <https://doi.org/10.1016/j.actamat.2019.05.041>
 20. J. Mohammadi, Y. Behnamian, A. Mostafaei and A.P. Gerlich, Tool Geometry, Rotation and Travel Speeds Effects on the Properties of Dissimilar Magnesium/Aluminum Friction Stir Welded Lap Joints, *Mater. Des.*, 2015, **75**, p 95–112. <https://doi.org/10.1016/j.matdes.2015.03.017>
 21. V.K. Yadav, V. Gaur and I.V. Singh, Effect of Post-Weld Heat Treatment on Mechanical Properties and Fatigue Crack Growth Rate in Welded AA-2024, *Mater. Sci. Eng. A*, 2019, **2020**(779), p 139116. <https://doi.org/10.1016/j.msea.2020.139116>
 22. S. Sinhmar and D.K. Dwivedi, A Study on Corrosion Behavior of Friction Stir Welded and Tungsten Inert Gas Welded AA2014 Aluminium Alloy, *Corros. Sci.*, 2018, **133**(January), p 25–35. <https://doi.org/10.1016/j.corsci.2018.01.012>
 23. W.M.T.E. D., J.C. Nicholas, M.G. Needham, Saffron Walden, H.P.T.-S. Murch, C.J. Dawes, Cambridge, and Cams, “FRICTION WELDING,” (United Kingdom), 1995
 24. R. Saravanakumar, T. Rajasekaran, C. Pandey and M. Menaka, Influence of Tool Probe Profiles on the Microstructure and Mechanical Properties of Underwater Friction Stir Welded AA5083 Material, *J. Mater. Eng. Perform.*, 2022, **31**(10), p 8433–8450. <https://doi.org/10.1007/s11665-022-06822-4>
 25. B. Li and Y. Shen, A Feasibility Research on Friction Stir Welding of a New-Typed Lap-Butt Joint of Dissimilar Al Alloys, *Mater. Des.*, 2012, **34**, p 725–731.
 26. R. Palanivel, P.K. Mathews, N. Murugan and I. Dinaharan, Effect of Tool Rotational Speed and Pin Profile on Microstructure and Tensile Strength of Dissimilar Friction Stir Welded AA5083-H111 and AA6351-T6 Aluminum Alloys, *Mater. Des.*, 2012, **40**, p 7–16. <https://doi.org/10.1016/j.matdes.2012.03.027>
 27. O. Hatamleh and A. DeWald, An Investigation of the Peening Effects on the Residual Stresses in Friction Stir Welded 2195 and 7075 Aluminum Alloy Joints, *J. Mater. Process. Technol.*, 2009, **209**(10), p 4822–4829.
 28. E.G. Cole, A. Fehrenbacher, N.A. Duffie, M.R. Zinn, F.E. Pfefferkorn and N.J. Ferrier, Weld Temperature Effects during Friction Stir Welding of Dissimilar Aluminum Alloys 6061–t6 and 7075–t6, *Int. J. Adv. Manuf. Technol.*, 2014, **71**, p 643–652.
 29. H.K. Pabandi, H.R. Jashnani and M. Paidar, Effect of Precipitation Hardening Heat Treatment on Mechanical and Microstructure Features of Dissimilar Friction Stir Welded AA2024-T6 and AA6061-T6 Alloys, *J. Manuf. Process.*, 2018, **31**, p 214–220. <https://doi.org/10.1016/j.jmapro.2017.11.019>
 30. R. Saravanakumar, T. Rajasekaran and C. Pandey, Optimisation of Underwater Friction Stir Welding Parameters of Aluminum Alloy AA5083 using RSM and GRA, *Proc. Inst. Mech. Eng. Part E J. Process. Mech. Eng.*, 2022 <https://doi.org/10.1177/09544089221134446>
 31. L. Giraud, H. Robe, C. Claudin, C. Desrayaud, P. Bocher and E. Feulvarch, Investigation into the Dissimilar Friction Stir Welding of AA7020-T651 and AA6060-T6, *J. Mater. Process. Technol.*, 2016, **235**, p 220–230.
 32. P.B. Srinivasan, W. Dietzel, R. Zettler, J.F. Dos Santos and V. Sivan, Effects of Inhibitors on Corrosion Behaviour of Dissimilar Aluminium Alloy Friction Stir Weldment, *Corros. Eng. Sci. Technol.*, 2007, **42**(2), p 161–167.
 33. M. Ilangoan, S.R. Boopathy and V. Balasubramanian, Microstructure and Tensile Properties of Friction Stir Welded Dissimilar AA6061-AA5086 Aluminium Alloy Joints, *Trans. Nonferrous Met. Soc. China*, 2015, **25**(4), p 1080–1090. [https://doi.org/10.1016/S1003-6326\(15\)63701-3](https://doi.org/10.1016/S1003-6326(15)63701-3)
 34. C.A.W. Olea, L. Roldo, J.F. dos Santos and T.R. Strohaecker, A Sub-Structural Analysis of Friction Stir Welded Joints in an AA6056 Al-Alloy in T4 and T6 Temper Conditions, *Mater. Sci. Eng. A*, 2007, **454–455**, p 52–62.
 35. Y.S. Sato, H. Kokawa, M. Enomoto and S. Jogan, Microstructural Evolution of 6063 Aluminum during Friction-Stir Welding, *Metall. Mater. Trans. A Phys. Metall. Mater. Sci.*, 1999, **30**(9), p 2429–2437.
 36. P.L. Niu, W.Y. Li, A. Vairis and D.L. Chen, Cyclic Deformation Behavior of Friction-Stir-Welded Dissimilar AA5083-to-AA2024 Joints: Effect of Microstructure and Loading History, *Mater. Sci. Eng. A*, 2018, **2019**(744), p 145–153.
 37. M. Cabibbo, H.J. McQueen, E. Evangelista, S. Spigarelli, M. Di Paola and A. Falchero, Microstructure and Mechanical Property Studies of AA6056 Friction Stir Welded Plate, *Mater. Sci. Eng. A*, 2007, **460–461**, p 86–94.
 38. A.P. Reynolds, W. Tang, Z. Khandkar, J.A. Khan and K. Lindner, Relationships between Weld Parameters, Hardness Distribution and Temperature History in Alloy 7050 Friction Stir Welds, *Sci. Technol. Weld. Join.*, 2005, **10**(2), p 190–199.
 39. Y. Chen, H. Wang, X. Wang, H. Ding, J. Zhao, F. Zhang and Z. Ren, Influence of Tool Pin Eccentricity on Microstructural Evolution and Mechanical Properties of Friction Stir Processed Al-5052 Alloy, *Mater. Sci. Eng. A*, 2018, **2019**(739), p 272–276.
 40. M. Guerra, C. Schmidt, J.C. McClure, L.E. Murr and A.C. Nunes, Flow Patterns during Friction Stir Welding, *Mater. Charact.*, 2002, **49**(2), p 95–101.
 41. K.N. Krishnan, On the Formation of Onion Rings in Friction, Stir Welds, *Mater. Sci. Eng. A*, 2002, **327**(2), p 246–251.
 42. C. Zhang, G. Huang, Y. Cao, Y. Zhu, W. Li, X. Wang and Q. Liu, Microstructure and Mechanical Properties of Dissimilar Friction Stir Welded AA2024-7075 Joints Influence of Joining Material Direction, *Mater. Sci. Eng. A*, 2019, **766**(March), p 138368. <https://doi.org/10.1016/j.msea.2019.138368>
 43. T. Azimzadegan and S. Serajzadeh, An Investigation into Microstructures and Mechanical Properties of AA7075-T6 during Friction Stir Welding at Relatively High Rotational Speeds, *J. Mater. Eng. Perform.*, 2010, **19**(9), p 1256–1263.
 44. J.Q. Su, T.W. Nelson and C.J. Sterling, Microstructure Evolution during FSW/FSP of High Strength Aluminum Alloys, *Mater. Sci. Eng. A*, 2005, **405**(1–2), p 277–286.
 45. S. Raja, M.R. Muhamad, M.F. Jamaludin and F. Yusof, A Review on Nanomaterials Reinforcement in Friction Stir Welding, *J. Mater. Res. Technol.*, 2020, **9**(6), p 16459–16487. <https://doi.org/10.1016/j.jmrt.2020.11.072>

46. P. Carlone and G.S. Palazzo, Influence of Process Parameters on Microstructure and Mechanical Properties in AA2024-T3 Friction Stir Welding, *Metallogr. Microstruct. Anal.*, 2013, **2**(4), p 213–222.
47. A. Heidarzadeh, S. Mironov, R. Kaibyshev, G. Çam, A. Simar, A. Gerlich, F. Khodabakhshi, A. Mostafaei, D.P. Field, J.D. Robson, A. Deschamps and P.J. Withers, Friction Stir Welding/Processing of Metals and Alloys: A Comprehensive Review on Microstructural Evolution, *Prog. Mater. Sci.*, 2020, **2020**(117), p 100752. <https://doi.org/10.1016/j.pmatsci.2020.100752>
48. Y.G. Kim, H. Fujii, T. Tsumura, T. Komazaki and K. Nakata, Three Defect Types in Friction Stir Welding of Aluminum Die Casting Alloy, *Mater. Sci. Eng. A*, 2006, **415**(1–2), p 250–254.
49. M. Paidar, K. Tahani, R. Vaira Vignesh, O.O. Ojo, H.R. Ezatpour and A. Moharrami, Modified Friction Stir Clinching of 2024–T3 to 6061–T6 Aluminium Alloy Effect of Dwell Time and Precipitation-Hardening Heat Treatment, *Mater. Sci. Eng. A*, 2020, **791**(June), p 139734. <https://doi.org/10.1016/j.msea.2020.139734>
50. T.R. McNelley, S. Swaminathan and J.Q. Su, Recrystallization Mechanisms during Friction Stir Welding/Processing of Aluminum Alloys, *Scr. Mater.*, 2008, **58**(5), p 349–354.
51. H. Suthar, A. Bhattacharya and S.K. Paul, Local Deformation Response and Failure Behavior of AA6061-AA6061 and AA6061-AA7075 Friction Stir Welds, *CIRP J. Manuf. Sci. Technol.*, 2020, **30**, p 12–24. <https://doi.org/10.1016/j.cirpj.2020.03.006>
52. K.V. Jata and S.L. Semiatin, Continuous Dynamic Recrystallization during Friction Stir Welding of High Strength Aluminum Alloys, *Scr. Mater.*, 2000, **43**(8), p 743–749.
53. M. Mahdi, H. Jamshidi, R. Jamaati and S. Amirkhanlou, Materials Characterization Effect of SiC Nanoparticles on the Microstructure and Texture of Friction Stir, *Mater Charact.*, 2019, **152**(March), p 169–179. <https://doi.org/10.1016/j.matchar.2019.04.020>
54. H. Jamshidi Aval, S. Serajzadeh, N.A. Sakharova, A.H. Kokabi and A. Loureiro, A Study on Microstructures and Residual Stress Distributions in Dissimilar Friction-Stir Welding of AA5086-AA6061, *J. Mater. Sci.*, 2012, **47**(14), p 5428–5437.
55. H. Jamshidi Aval, Influences of Pin Profile on the Mechanical and Microstructural Behaviors in Dissimilar Friction Stir Welded AA6082-AA7075 Butt Joint, *Mater. Des.*, 2015, **67**, p 413–421. <https://doi.org/10.1016/j.matdes.2014.11.055>
56. A.A.M. da Silva, E. Arruti, G. Janeiro, E. Aldanondo, P. Alvarez and A. Echeverria, Material Flow and Mechanical Behaviour of Dissimilar AA2024-T3 and AA7075-T6 Aluminium Alloys Friction Stir Welds, *Mater. Des.*, 2011, **32**(4), p 2021–2027. <https://doi.org/10.1016/j.matdes.2010.11.059>
57. S.T. Amancio-Filho, S. Sheikhi, J.F. dos Santos and C. Bolfarini, Preliminary Study on the Microstructure and Mechanical Properties of Dissimilar Friction Stir Welds in Aircraft Aluminium Alloys 2024–T351 and 6056–T4, *J. Mater. Process. Technol.*, 2008, **206**(1–3), p 132–142.
58. M. Koilraj, V. Sundareswaran, S. Vijayan and S.R. Koteswara Rao, Friction Stir Welding of Dissimilar Aluminum Alloys AA2219 to AA5083 Optimization of Process Parameters Using Taguchi Technique, *Mater. Des.*, 2012, **42**, p 1–7. <https://doi.org/10.1016/j.matdes.2012.02.016>

Publisher's Note Springer Nature remains neutral with regard to jurisdictional claims in published maps and institutional affiliations.

Springer Nature or its licensor (e.g. a society or other partner) holds exclusive rights to this article under a publishing agreement with the author(s) or other rightsholder(s); author self-archiving of the accepted manuscript version of this article is solely governed by the terms of such publishing agreement and applicable law.